NASA Technical Memorandum 81964

FINITE ELEMENT ANALYSIS OF INSTABILITY-RELATED DELAMINATION GROWTH

John D. Whitcomb

March 1981

NASA

National Aeronautics and
Space Administration

Langley Research Center
Hampton, Virginia 23665

SUMMARY

A parametric study of postbuckled through-width delaminations in laminated coupons was performed. A finite element analysis was developed to analyze the coupons as a combination of linear and geometrically nonlinear components. Because most of the coupon configuration studied behaves linearly, the mixed linear and nonlinear analysis greatly reduced computational costs. The analysis was verified by comparing numerical with exact solutions for simple hypothetical problems. In addition, measured lateral deflections of postbuckled through-width delaminations in laminated coupons were compared with predicted deflections. In the parametric study, stress distributions and strain-energy release rates were calculated for various delamination lengths, delamination depths, applied loads, and lateral deflections. Also, a small number of coupons with through-width delaminations were fatigue tested to obtain delamination growth data. Calculated strain-energy release rates were compared with the observed growth rates to determine the relative importance of the Mode I and Mode II components of energy release. G_I was shown to dominate the growth process.

NOMENCLATURE

A	area
a	half-length of delamination
C_{ijkl}	material stiffness coefficients
E_1, E_2	Young's modulus in x_1 and x_2 directions
G_{12}	shear modulus
G_I	Mode I strain-energy release rate

G_{II}	Mode II strain-energy release rate
I	moment of inertia
$(K_o)_{mn}^{\theta\lambda}$	element linear stiffness coefficients
$(K_L)_{mn}^{\theta\lambda}$	element large displacement stiffness coefficients
$(K_T)_{mn}^{\theta\lambda}$	element tangential stiffness coefficients
$(K_\sigma)_{mn}^{\theta\lambda}$	element geometric stiffness coefficients
ℓ	length of column
N^θ	polynomial interpolation function for node θ
N	applied load cycles
P	applied load
P_n^λ	applied load in x_n direction at node λ
t	thickness of buckled region
U	strain energy
μ_i	displacement in x_i direction
μ_i^θ	displacement in x_i direction at node θ
w	width of specimen
W	potential energy of external loads
x_a	axial projection of buckled column
x_1, x_2	rectangular Cartesian coordinates
y_a	lateral deflection of buckled column
δ	lateral deflection
$\bar{\delta}$	specified lateral deflection
δ_{ij}	Kronecker delta
ϵ_{ij}	stain components

2

ν_{21} Poisson's ratio

Π total potential energy

σ_{ij} stress components

ψ_n^λ residual force in x_n direction at node λ

Range of indices:

Lowercase Latin indices   1, 2

Lowercase Greek indices   1, number of nodes per element

INTRODUCTION

Local buckling of delaminated plies in composite laminates can precipitate rapid delamination growth and structural collapse. To assess the criticality of a delamination, an analysis is needed to predict the rate of instability-related delamination growth. The logical evolution of a comprehensive analysis starts with a thorough understanding of instability-related delmaination growth in simple configurations. One of the simplest configurations is a through-width delamination in a laminated coupon subjected to compression loads (fig. 1).

Accordingly, the objective of this paper was to investigate instability-related growth of a through-width delamination in a laminated coupon. The investigation involved both analysis and experiments. In the analytical effort an efficient, geometrically-nonlinear finite element stress analysis was developed. The analysis was verified by comparing numerical with exact solutions for simple problems. In addition, measured lateral deflections of postbuckled through-width delaminations in laminated coupons were compared with predicted deflections. The analysis was used to perform a parametric study of postbuckled through-width delaminations. Lateral deflections, stress

3

distributions, and strain-energy release rates were calculated for various delamination lengths, delamination depths, and applied loads. A small number of specimens with through-width delaminations were fatigue tested to obtain delamination growth data. These specimens consisted of unidirectional graphite/ epoxy bonded to aluminum. Observed delamination growth rates were qualitatively correlated with calculated strain-energy release rates to determine the relative importance of the Mode I and Mode II components of energy release.

ANALYSIS

A two-dimensional finite element analysis was developed to study post-buckling of through-width delaminations in a laminated coupon (fig. 1). The analysis accounts for geometric nonlinearity, which is caused by the large rotation in the buckled region. Development of the analysis is outlined in the following paragraphs.

Development of Governing Equations

The governing nonlinear equations for individual elements can be derived using the principle of minimum total potential energy. The total potential energy, Π, is given by equation (1) (ref. 1).

$$\Pi = U - W = \frac{W}{2} \int \sigma_{ij} \varepsilon_{ij} \, dA - W \tag{1}$$

Geometric nonlinearity is included by using the nonlinear strain-displacement relations, (ref. 2) in equation (1).

$$\varepsilon_{ij} = \frac{1}{2} \left(\frac{\partial \mu_i}{\partial x_j} + \frac{\partial \mu_j}{\partial x_i} + \frac{\partial \mu_r}{\partial x_i} \frac{\partial \mu_r}{\partial x_j} \right) \tag{2}$$

4

The displacements μ_1 and μ_2 within an element are approximated with interpolation functions, that is

$$\mu_i = N^\theta \mu_i^\theta \tag{3}$$

Using equations (1), (2), and (3) to calculate and minimize Π with respect to μ_i^θ yields

$$w \int \sigma_{ij} \frac{\partial \epsilon_{ij}}{\partial \mu_n^\lambda} \, dA = P_n^\lambda \tag{4}$$

Equations (4) are the set of governing nonlinear equations for the element. The equations for all elements are assembled to form a system of governing equations. If a region behaves linearly, equations (4) simplify to linear equations.

The assembled nonlinear governing equations are solved iteratively using the Newton-Raphson method (ref. 1). To implement this method, the assembled tangential stiffness matrix is needed. The assembled tangential stiffness matrix is obtained by combining the individual element stiffness matrices. The element tangential stiffness matrix is obtained from equation (4) by partial differentiation as follows:

$$(K_T)_{mn}^{\theta\lambda} = w \frac{\partial}{\partial \mu_m^\theta} \left(\int \sigma_{ij} \frac{\partial \epsilon_{ij}}{\partial \mu_n^\lambda} \, dA \right) \tag{5}$$

5

Performing the differentiation and simplifying results in

$$(K_T)_{mn}^{\theta\lambda} = (K_0)_{mn}^{\theta\lambda} + (K_L)_{mn}^{\theta\lambda} + (K_\sigma)_{mn}^{\theta\lambda} \tag{6}$$

where

$$(K_0)_{mn}^{\theta\lambda} + (K_L)_{mn}^{\theta\lambda} = w \int C_{ijk\ell} \frac{\partial\epsilon_{k\ell}}{\partial\mu_m^\theta} \frac{\partial\epsilon_{ij}}{\partial\mu_n^\lambda} dA$$

and

$$(K_\sigma)_{mn}^{\theta\lambda} = w \int \delta_{mn}\sigma_{ij} \frac{\partial N^\lambda}{\partial x_i} \frac{\partial N^\theta}{\partial x_j} dA$$

$(K_0)_{mn}^{\theta\lambda}$, $(K_L)_{mn}^{\theta\lambda}$, and $(K_\sigma)_{mn}^{\theta\lambda}$ are the linear, large displacement, and geometric stiffness matrices, respectively.

The elements used in the analysis were four-node, isoparametric quadrilaterals. To improve the performance of the elements in modeling bending deformation, a reduced numerical integration scheme (ref. 3) was used to evaluate the element stiff, ss matrices. Details of the reduced integration scheme are given in appendix A.

In postbuckling analysis of a through-width delamination in a laminated coupon, the assembled tangential stiffness matrix may become singular. This problem arises because the buckled region has a small lateral stiffness (fig. 2(a)). The calculated stiffness is a function of the current displacements and stresses. Because the actual lateral stiffness is so small, errors in the estimate of displacements and stresses significantly affect the estimate

6

of the lateral stiffness. In fact, during the iterative solution of the governing nonlinear equations, the current estimate of the displacements and stresses may be such that the buckled region has no lateral stiffness. The result is a singular stiffness matrix.

To avoid a singular tangential stiffness matrix during the iterative solution, an incremental displacement procedure (ref. 5) was used. This procedure involves modifying the original model (fig. 2(a)) by specifying the peak lateral displacement, $\bar{\delta}$, (fig. 2(b)). This modified model is equivalent to the original if the support reaction (R) is equal to zero. Because R is a nonlinear function of the applied load (P), an iterative solution is required to determine the magnitude of P. The correct P is that which corresponds to a zero support reaction. The initial estimate of P, which need not be very accurate, is part of the input data. Hence, the unknowns consist of nodal displacements and the magnitude of the applied load. The load-deflection relationship was determined by examining a range of $\bar{\delta}$.

Computer Implementation

The computer program was designed to perform analysis by substructures (ref. 6). Besides reducing computer memory requirements, substructuring facilities analysis of a structure as a combination of linear and nonlinear components. For the configuration studied in this paper (fig. 1), linear analysis is appropriate for all regions except the buckled region. By substructuring into linear and nonlinear regions, expensive iterative solution techniques are needed for only a fraction of the equations.

A disadvantage of substructuring is the additional bookkeeping required. However, the substructuring scheme used herein minimizes this

additional bookkeeping, yet is simple to implement. This scheme is described below.

As an example of the substructuring technique, consider figure 3. The rectangular region is shown divided into two substructures. The first has 48 nodes; the second has 36 nodes. After assembling the stiffness matrix and load vector for substructure 1, Gaussian elimination is used to eliminate nodes 1 to 42. The reduced stiffness matrix and load vector remain. The remaining nodes can be considered the constitutive nodes for a "super element." The nodes for the super element (originally numbered 43 to 48) are given new numbers (as input data) that depend on the numbering scheme in substructure 2. In this example, the new constitutive nodes would be 36-35-34-33-32-31. The next step is to assemble the stiffness matrix and load vector for substructure 2. To account for the interaction between substructures 1 and 2, the stiffness matrix and load vector for the "super element" are added to the assembled stiffness matrix and load vector, respectively, for the elements within substructure 2.

In analyzing the laminated coupon, the reduced stiffness matrix and load vector for the linear region was calculated once and retained in memory. Each time the tangential stiffness matrix and load vector for the nonlinear region were assembled, the interaction with the linear region was accounted for by adding the reduced stiffness matrix and load vector from the linear region. In the current study, this procedure reduced the number of equations solved iteratively from 1626 to 182.

The computer program was verified by analyzing two problems with exact solutions. Details are given in appendix B.

Finite Element Models

The laminated coupon which was used in the experimental portion of this study consisted of graphite/epoxy bonded to 2024-T3 aluminum. This configuration was selected to simplify fabrication of specimens used in the experimental part of the study.

A typical finite element mesh for the test coupon is shown in figure 4. Because of symmetry only half of the coupon was modeled. The adhesive was not included in the analytical model. The model contained four substructures with a total of 813 nodes and 740 four-node isoparametric elements. This particular mesh is for the case $2a = 25$ mm, $t = 0.76$ mm. Similar meshes were used for other delamination lengths (2a) and depths (t). In general the mesh around the crack tip (i.e., delamination front) remained unchanged. However, for a delamination depth of 0.25 mm (0.01 in.) the mesh at the crack tip was slightly more refined than that shown in the figure.

Boundary conditions are indicated in figure 4. Because of symmetry, μ_1 is zero along the line $x_1 = -a$. At $x_1 = -a$, $x_2 = 6$ mm, μ_2 is set to zero to prevent rigid body motion. At $x_1 = a$, $x_2 = 6$ mm, μ_2 is set to zero.

Because the rotations are small in substructure 1 to 3, this region was assumed to behave linearly. Substructure 4 was assumed to behave nonlinearly.

Material Properties

Engineering material properties for the graphite/epoxy and aluminum were assumed to be

Aluminum: $E_1 = E_2 = 67$ GPa (9.7×10^6 PSI)

$G_{12} = 25$ GPa (3.6×10^6 PSI)

$\nu_{12} = 0.33$

Graphite/Epoxy: $E_1 = 140$ GPa $(20 \times 10^6$ PSI$)$

$E_2 = 14$ GPa $(2.0 \times 10^6$ PSI$)$

$G_{12} = 5.9$ GPa $(0.85 \times 10^6$ PSI$)$

$\nu_{21} = 0.021$

The relationships between these engineering constants and the stiffness coefficients $C_{ijk\ell}$ may be found in reference 7. Plane stress conditions were assumed for the analysis.

EXPERIMENTAL PROCEDURE

The specimen configuration is shown in figure 5. Four-ply unidirectional graphite/epoxy was bonded to 2024-T3 AL with EA934 adhesive. The adhesive was cured at room temperature. To simulate a delamination, teflon tape was used to prevent bonding in the central part of the specimen.

Some of the specimens were loaded statically so that lateral deflections could be measured. Lateral deflections were measured with a micrometer. Five fatigue specimens were tested under constant-amplitude, load-controlled, sinusoidal, axial loading. The loading was compression-compression with a load ratio (R) of 20 and a frequency of 10 Hz. A scale was positioned next to the specimen and was viewed with a hand-held telescope to measure delamination lengths.

RESULTS AND DISCUSSION

Instability-related delamination growth was studied analytically and experimentally. The analytical study of stress distributions and strain energy release rates is discussed first. Then comparisons are drawn between analytical results and observed experimental behaviors.

10

Parametric Analysis

Figures 6 and 7 show stress distributions near the delamination front in a laminate with $2a = 38$ mm and $t = 0.51$ mm. The averaging techniques used in calculating these stresses is illustrated in the sketches below. Slightly different techniques were used for the distributions through the thickness and along the interface. Through the thickness, point stresses within the same element were averaged. Along the interface, point stresses in elements on both sides of the interface were averaged. Stresses were evaluated at the Gaussian quadrature points for both cases. Figure 6 shows the interlaminar

$+$ Point stresses used in averaging

$(+ \ +)$ Group of point stresses averaged together

Through the thickness

Along interface
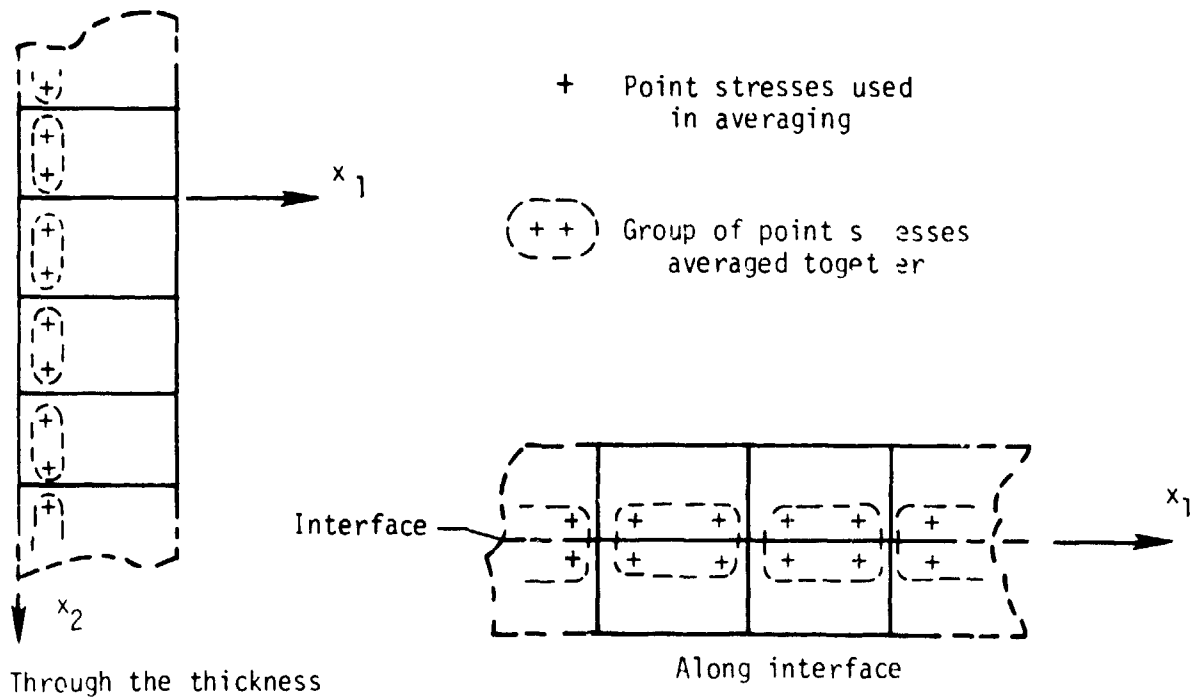
normal (σ_{22}) and shear (σ_{12}) stress distributions through the thickness of the specimen $(x_1 = 0.0051$ mm) for three different loads. The stresses are plotted to different scales because the peak values are quite different. Both the

11

σ_{22} and σ_{12} distributions exhibit very steep gradients near the crack tip, suggesting a singularity. As the load increases from $P = 7.68$ KN to 31.7 KN, the shape of the σ_{12} distribution remains essentially the same, only the amplitude changes. In contrast, the σ_{22} distribution changes shape dramatically from $P = 15.7$ KN to $P = 31.7$ KN.

Figure 7 shows the interlaminar stress distributions along the interface between the graphite/epoxy and the aluminum ($x_2 = 0.51$ mm) for the three different loads. As in the through-the-thickness distributions, the shear stress σ_{12} distributions for the three cases have very similar shape. The normal stress σ_{22} distributions along the interface do not exhibit any dramatic change like that shown in figure 6. However, neither σ_{22} nor σ_{12} in figure 6 or 7 vary linearly with applied load or lateral deflection.

Because of the apparent singularity at the crack tip, the magnitude of the calculated stresses at the crack tip have little meaning. Use of a more refined mesh would result in higher calculated values. In contrast, calculated strain-energy release rates represent the product of nodal forces and displacements near the crack tip and are much less sensitive to mesh refinement. Also, for the same level of accuracy, a cruder mesh suffices for the energy calculation, which is based on the product of forces and displacements, than for the stress calculation, which is based on derivatives of displacement. Furthermore, there is no need to use any singular stress element formulation to obtain the strain energy release rates (ref. 6). Hence, strain-energy release rates are convenient to use to characterize delamination growth. For this reason, the remainder of this parametric study concentrates on how various parameters affect strain-energy release rates. The technique for

12

calculating strain-energy release rates is described in reference 10 and briefly in appendix B.

Figure 8 through 10 show the relationship between delamination length, applied load, lateral deflection, and Mode I and Mode II strain-energy release rates (G_I and G_{II}, respectively). Lateral deflections are examined because intuitively one might expect the severity of the interlaminar stresses to be related to the degree of postbuckling deflections.

Figure 8 illustrates the nonlinear relationships between load, delmaination length (2a), and G_I. G_I first increases then decreases with increasing load. If the system were linear, G_I would have increased monotonically in proportion to the square of the load. The shorter delaminations have the larger values of peak G_I. However, the longer delaminations show a nonzero G_I at lower loads.

Figure 9 shows the relationship between lateral deflections, delamination length, and G_I. Contrary to intuition, G_I does not increase monotonically with lateral deflection. In fact, G_I is zero at a lateral deflection of approximately 1.5 mm. Furthermore, the maximum values of G_I for all the delamination lengths occurs at a δ of approximately 0.76 mm.

The trends shown in figures 8 and 9 can be explained by considering the load transfer near the crack tip. After the delaminated region buckles, an increase in applied load (and lateral deflection) causes essentially no change in the load carried by the buckled region (region C in the sketch). However, the load carried by region A continues to increase with increased load. Hence, load must be transferred from A to D. The eccentricity in the load path causes a moment which tends to close the crack tip. Simultaneously, the lateral deflection causes a moment which tends to open the crack tip. The

13
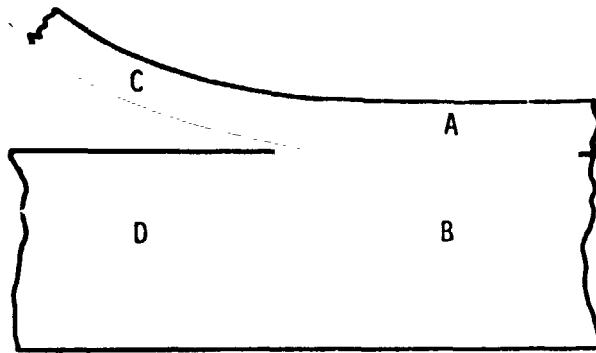
interaction of these processes causes G_I to first increase then decrease with increasing load and lateral deflection.

Figure 10 shows the effect of delamination length and load on G_{II}. Results are shown only for loads less than that required to close the crack tip in the direction normal to the crack surfaces. The current analysis is not valid for higher loads, since no provision is made to keep the crack surfaces from overlapping. The figure shows that G_{II} increases monotonically with load. The curves for the different delamination lengths seem to be coalescing at the higher load levels. Because lateral deflection also increases monotically with load, G_{II} increases monotonically with lateral deflection.

Recall that G_I did not increase monotonically with load. Hence, the ratio $G_I:G_{II}$ varies with load. For a linear system this ratio would have been independent of the load. Note also that for the cases examined, G_{II} is in general much larger than G_I.

Figures 11 and 12 show that G_I and G_{II} are very sensitive to the depth (t) of the delamination. The trends are similar to those in figures 8 and 10 (in which delamination length was varied), except the peak values of

G_I increase as t increases. Intuition suggests that G_I is related to the bending stiffness of the buckled region. Hence, the results are not surprising since the bending stiffness varies directly as t^3 and inversely as $(2a)^2$.

Comparison of Analytical and Experimental Results

The only direct comparison of analytical results and experiments was for lateral deflections. As shown in figure 13, the analysis reflects the actual behavior of the specimen.

Figure 14 shows delamination growth rates for various delamination lengths at maximum compressive loads of 17.8 KN and 26.7 KN (4000 lbs and 6000 lbs, respectively). Three specimens were tested at 17.8 KN and four were tested at 26.7 KN. (Note that specimens 2 and 3 were tested at both load levels.) There is considerable scatter in the data. However, one obvious trend is the rapid slowing of delamination growth as the delamination lengthens.

Figure 15 illustrates how G_I, G_{II}, and delamination growth rate vary as a delamination grows. The G_I and G_{II} curves were derived from the curves in figures 8 and 10, respectively. The growth data are from figure 11(a). Note that both G_I and the growth rate first increase then decrease with delamination extension; G_{II} increases monotonically and does not reflect the change in growth rate. Although G_{II} is numerically much larger than G_I, delamination growth appears to be dominated by the Mode I component of stress.

CONCLUDING REMARKS

A parametric analytical study of instability-related delamination growth in laminated coupons was performed using a specially designed finite-element program. The analysis was designed to analyze coupons as a combination of linear and nonlinear regions. The program was verified by analyzing two

problems with exact solutions. In addition, comparison of measured and predicted lateral deflections of postbuckled through-width delaminations showed the analysis reflected actual specimen behavior. A small number of specimens were fatigue tested to obtain delmaination growth data. Calculated strain-energy release rates were qualitatively correlated with the observed growth rates to determine the relative importance of the Mode I and Mode II components of strain-energy release rates.

Load transfer near the delamination was very complex. Interlaminar stresses were not a simple function of applied load or lateral deflection. Very steep gradients in the calculated stresses at the delamination front suggested the presence of a stress singularity. Hence, the peak values of interlaminar stresses have little meaning, since they depend on mesh refinement. In contrast, strain-energy-release rates are much less sensitive than the calculated stresses to mesh refinement. Consequently, strain-energy-release rates (rather than stresses) were examined for various delamination lengths, delamination depths, and loads.

Calculated strain-energy-release rates for Mode I and Mode II crack extension (G_I and G_{II}, respectively) were very sensitive to delamination length, delamination depth, and load level. G_I increased with increasing load and lateral deflection initially, but then decreased. G_{II} increased monotonically with increasing load. If the structure had responded linearly, G_I would have increased monotonically with the square of the load, and the ratio G_I/G_{II} would have remained constant. For any arbitrary lateral deflection, G_I was greater for the shorter and deeper delamination. For an arbitrary remote load, G_I was not necessarily greater or smaller for the shorter and deeper delaminations.

16

Qualitative correlation of calculated G_I ond G_{II} values with observed delamination growth rates showed that delamination growth is dominated by G_I, even though G_{II} may be numerically much larger. Because G_I is not a simple function of delamination length, delamination depth, applied load, or lateral deflection, predicting growth rates from a limited delamination growth data base is expected to be difficult. Furthermore, these predictions will likely be susceptible to large errors.

APPENDIX A

REDUCED NUMERICAL INTEGRATION

Many two-dimensional finite elements are inadequate in modeling pure bending deforma_ions. The poor performance is due to the inability of these elements to represent pure bending deformations. In pure bending, the shear strain ϵ_{12} is zero. However, when displacements corresponding to pure bending are prescribed at the nodes, these elements develop nonzero shear strain (refs. 3 and 4). This shear strain, called parasitic shear, causes the element to be excessively stiff.

Selective reduced integration of terms related to shear distortion can dramatically improve the performance of two-dimensional elements which exhibit parasitic shear (refs 3 and 4). In the finite element program developed for the current study, full integration refers to four-point Gauss integration; reduced integration refers to single point integration at the element centroid. Selective reduced integration for linear analysis is discussed in references 3 and 4. For nonlinear analysis, reduced integration schemes are also needed for the large displacement matrix (K_L), the geometric stiffness matrix (K_σ), and the residual vector (ψ). Terms which should be calculated using reduced integration are identified below.

Expressions for stiffness matrices and the residual vector are given by equations (A1) through (A3).

$$(K_o)_{mn}^{\theta\lambda} + (K_L)_{mn}^{\theta\lambda} = t \int C_{ijk\ell} \frac{\partial \epsilon_{k\ell}}{\partial \mu_m^\theta} \frac{\partial \epsilon_{ij}}{\partial \mu_n^\lambda} \, dA \qquad (A1)$$

18

APPENDIX A

$$(K_\sigma)_{mn}^{\theta\lambda} = t \int \delta_{mn}\sigma_{ij} \frac{\partial N^\lambda}{\partial x_i} \frac{\partial N^\theta}{\partial x_j} dA \qquad (A2)$$

$$\psi_n^\lambda = t \int \sigma_{ij} \frac{\partial \epsilon_{ij}}{\partial \mu_n^\lambda} dA - P_n^\lambda \qquad (A3)$$

In equations (A1) and (A3) the partial derivatives of shear strains are evaluated at the reduced integration points. In equations (A2) and (A3) the shear stress is the current shear stress at the element centroid. To be confident in choosing the remaining shear-related terms in equation (A2), the derivation of the geometric stiffness matrix must be examined. The geometric stiffness matrix is one component of the tangential stiffness matrix, K_T, where

$$(K_T)_{mn}^{\theta\lambda} = t \frac{\partial}{\partial \mu_m^\theta} \left[\int \sigma_{ij} \frac{\partial \epsilon_{ij}}{\partial \mu^\lambda} dA \right] \qquad (A4)$$

When the differentiation is performed, one of the terms is

$$t \int \sigma_{ij} \frac{\partial}{\partial \mu_m^\theta} \left(\frac{\partial \epsilon_{ij}}{\partial \mu_n^\lambda} \right) dA \qquad (A5)$$

19

APPENDIX A

This term, when expanded and simplified, becomes the right hand side of equation (A2). The products of derivatives, $\partial N^\lambda/\partial x_i \quad \partial N^\theta/\partial x_j$, are derived from the term $\dfrac{\partial}{\partial \mu_m^\theta}\left(\dfrac{\partial \epsilon_{ij}}{\partial \mu_n^\lambda}\right)$. Comparison of indices shows that the product of derivatives is a shear related term if $i \neq j$. Hence, in equation (A2) all products in which $i \neq j$ are calculated by reduced integration.

APPENDIX B

VERIFICATION OF ANALYSIS

Two problems with exact solutions were analyzed to verify the finite element analysis. The first problem involved large deflection of a column. This problem was used to check the modeling of geometric nonlinearity. The second problem studied involved a double cantilever beam. This configuration was used to check the strain-energy release rate calcualtion.

A schematic of the large-deflection column problem is shown in figure B1. The solution, given in reference 8, is in terms of complete elliptic integrals. A truncated series representation for the integrals was used to derive the following relationships

$$P = \frac{\pi^2 E_1 I}{4\ell^2} \left(1 + \frac{\rho^2}{2}\right) \tag{B1}$$

$$x_a = \ell \left[\frac{4 - 3\rho^2}{4 + \rho^2}\right] \tag{B2}$$

$$y_a = \frac{4\rho\ell}{\pi} \tag{B3}$$

where

$\rho = \sin \alpha/2$

P = load in column

APPENDIX B

x_a = projection of deformed column on x axis

y_a = lateral deflection

Shear effects were ignored because of a large length/thickness ratio ($\ell/t = 50$). In the finite element analysis, particular values of lateral deflection (y_a) were specified. Corresponding values of x_a and P were calculated by the analysis. Material properties used in the analysis were

$$E_1 = 140 \text{ GPa } (20 \times 10^6 \text{ PSI})$$
$$E_2 = 14 \text{ GPa } (2.0 \times 10^6 \text{ PSI})$$
$$G_{12} = 5.9 \text{ GPa } (0.85 \times 10^6 \text{ PSI})$$
$$\nu_{21} = 0.021$$

Dimensions are shown on the finite element mesh used (fig. B2). This mesh was the same as one of the meshes used in the main text. Substructures 1 and 2 here correspond to substructures 3 and 4 in the main text. Linear analysis was used for substructure 1 and nonlinear analysis for substructure 2.

Calculated loads and axial shortening for three values of lateral deflections are listed in the following table.

	EXACT			FINITE ELEMENT	
y_a/ℓ	$(\ell - x_a)/\ell$	$[(\ell - x_a)/\ell]_{CORR}$	P/P_e^*	$(\ell - x_a)/\ell$	P/P_e^*
0.005	1.54×10^{-5}	9.77×10^{-5}	1.00	9.82×10^{-5}	1.00
.05	1.54×10^{-3}	1.62×10^{-3}	1.00	1.62×10^{-3}	1.01
.10	6.16×10^{-3}	6.24×10^{-3}	1.00	6.27×10^{-3}	1.01

$$^*P_e = \text{Euler buckling load} = \frac{\pi^2 E_1 I}{4\ell^2}$$

For small lateral deflections the axial shortening is primarily due to axial strain. The column labeled $[(\ell - x_a)/\ell]_{CORR}$ has the value of $[(\ell - x_a)/\ell]$ corrected for the average axial strain (which is P/AE). The finite element and exact solutions agree very well for both the loads and the axial shortening.

To check the strain energy release rate calculation, the double cantilever beam configuration in figure B3 was analyzed. Loading was in the form of specified lateral displacement, δ. A crack closure technique similar to that reported in reference 9 was used to calculate strain energy release rates. The forces transmitted through the node at the crack tip and the relative displacements of the two nodes on the crack boundary closest the crack tip node were used to calculate the energy required to close the crack. If an element is considered to behave nonlinearly, these nodal forces must be calculated from equation (B4)

$$P_n^\lambda = t \int \sigma_{ij} \frac{\partial \epsilon_{ij}}{\partial \mu_n^\lambda} \, dA \qquad\qquad (B4)$$

If an element is considered to behave linearly, the nodal forces are calculated from the linear stiffness matrix and nodal displacements. For all the results reported in this paper, the elements around the crack tip were assumed to behave linearly. The finite element mesh and material properties were the same as used for the column. Because of symmetry only half of the double cantilever beam was modeled. Linear analysis was used for substructure 1 and nonlinear analysis for substructure 2. For this problem, the difference between linear and nonlinear analysis of substructure 2 is negligible except for large lateral displacements.

For the double cantilever beam, $G_{II} = 0$ because of symmetry. For small lateral displacements, the closed form expression for G_I can be shown to be

$$G_I = \frac{9E_1 I \delta^2}{\ell^4} \qquad\qquad (B5)$$

For the case $\delta = 0.25$ mm, equation (B5) yields a value of 2.10 joules/m^2. The finite element solution yielded $G_I = 2.12$ joules/m^2, which agrees very well with the exact value.

REFERENCES

1. Zienkiewicz, O. C.: The Finite Element Method in Engineering Science, 2nd Ed., McGraw-Hill, New York, 1971.

2. Novozhilov, V. V.: Theory of Elasticity, translated by J. K. Lusher, Pergamon Press, New York, 1961.

3. Pawsey, S. F.; and Clough, R. W.: Improved Numerical Integration of Thick Shell Finite Elements, in International Journal for Numerical Methods in Engineering, Vol. 3, 1971, pp. 575-586.

4. Zienkiewicz, O. C.; Taylor, R. L.; and Too, J. M.: Reduced Integration Technique in General Analysis of Plates and Shells, in International Journal for Numerical Methods in Engineering, Vol. 3, 1971, p. 275-290.

5. Zienkiewicz, O. C.: Incremental Displacement in Non-linear Analysis, in International Journal for Numerical Methods in Engineering, Vol. 3, 1971, pp. 587-592.

6. Weaver, W., Jr.: Computer Programs for Structural Analysis, Van Nostrand, Princeton, New Jersey, 1967.

7. Noor, A. K.; and Mathers, M. D.: Shear-Flexible Finite-Element Models of Laminated Composite Plates and Shells, NASA TN D-8044, Dec. 1975, (Appendix B).

8. Wang, A. S. D.; and Crossman, F. W.: Initiation and Growth of Transverse Cracks and Edge Delamination in Composite Laminates, Part 1. Energy Method, Journal of Composite Materials Supplemental Volume, 1980, pp. 71-87.

9. Timoshenko, S. P.; and Gere, J. M.: Theory of Elastic Stability, 2nd Ed., McGraw-Hill, New York, 1961, pp. 76-81.

10. Rybicki, E. F.; and Kanninen, M. F.: A Finite Element Calcualtion of Stress Intensity Factors by a Modified Crack Closure Integral, Engineering Fracture Mechanics, 1977, Vol. 9, pp. 931-938.
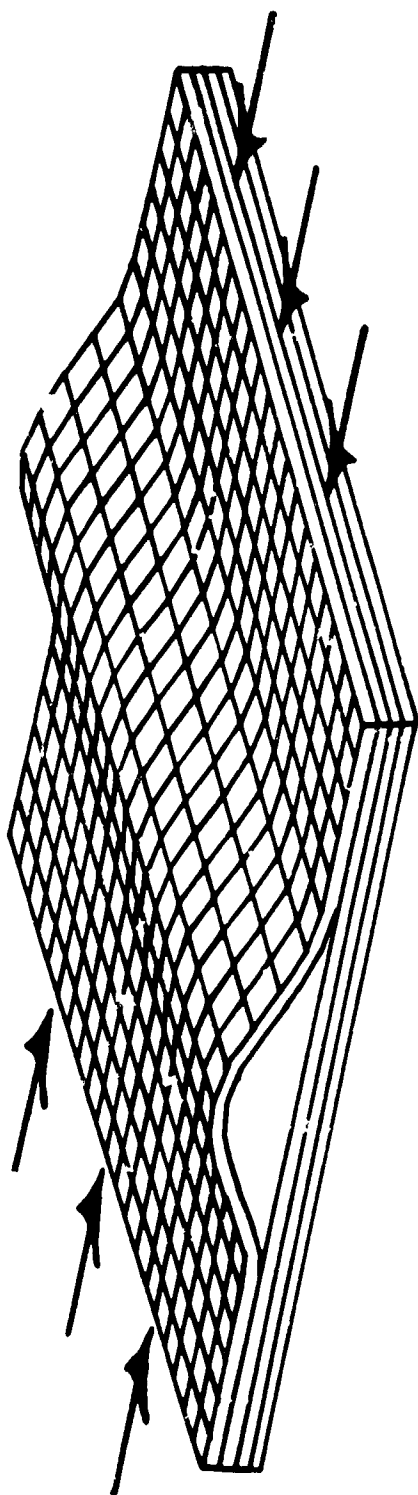
Figure 1.- Local buckling of laminate with a through-width delamination.
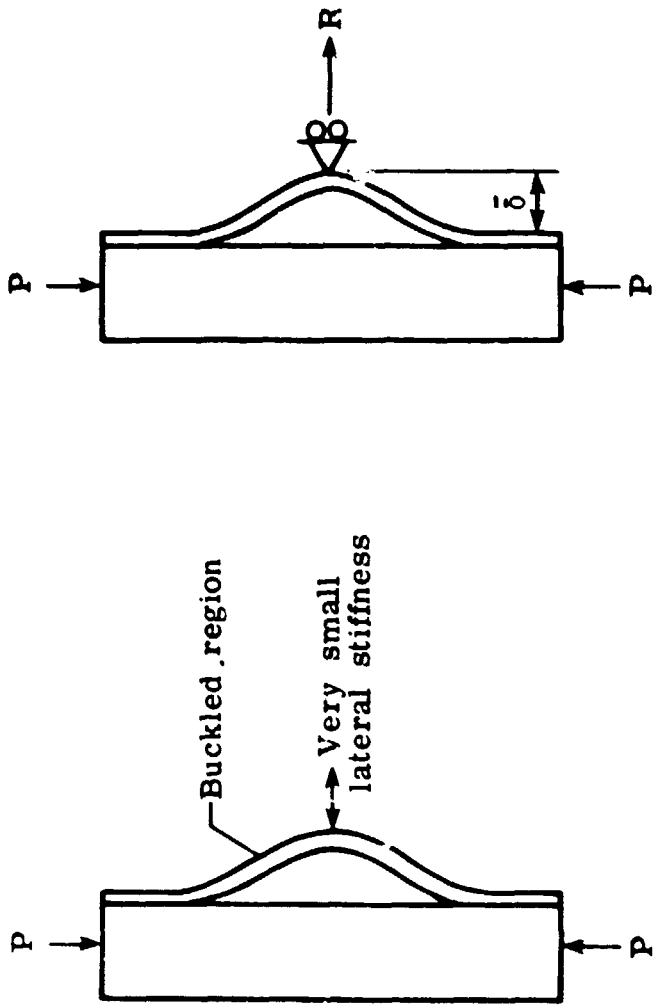
(a) Original configuration.   (b) Configuration with fixed lateral deflection.

Figure 2.- Modification of analytical model to avoid singular stiffness matrix.

27
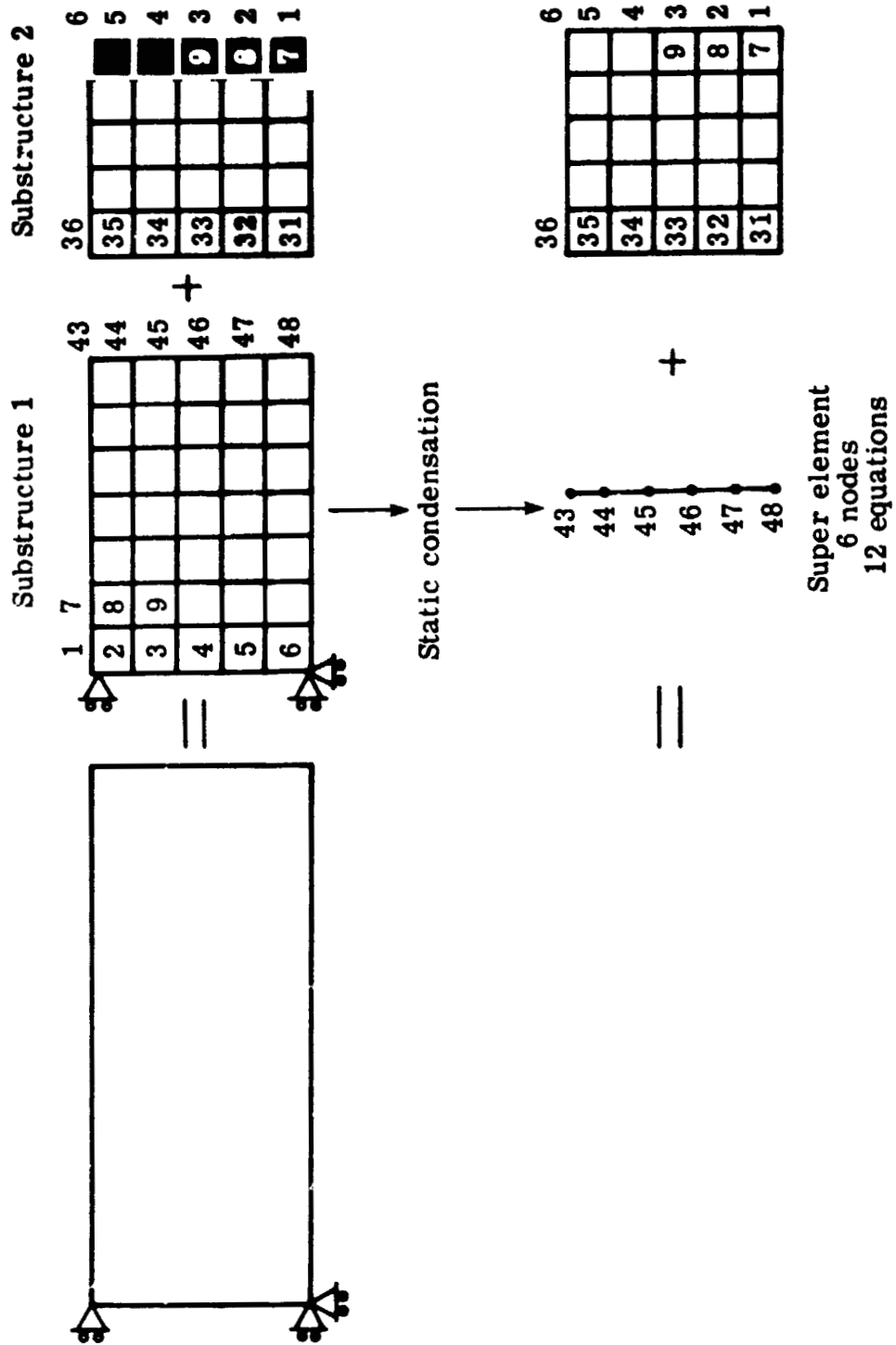
Figure 3.- Illustration of substructuring technique.

Substructure 1 $-a \leq x_1 \leq 0$ mm; $0 \leq x_2 \leq 6.0$ mm

Substructure 2 $0 \leq x_1 \leq 13$ mm; $-t \leq x_2 \leq 6.0$ mm

Substructure 3 $-.56 \leq x_1 \leq 0$ mm; $-t \leq x_2 \leq 0$ mm

Substructure 4 $-a \leq x_1 \leq -.56$ mm; $-t \leq x_2 \leq 0$ mm
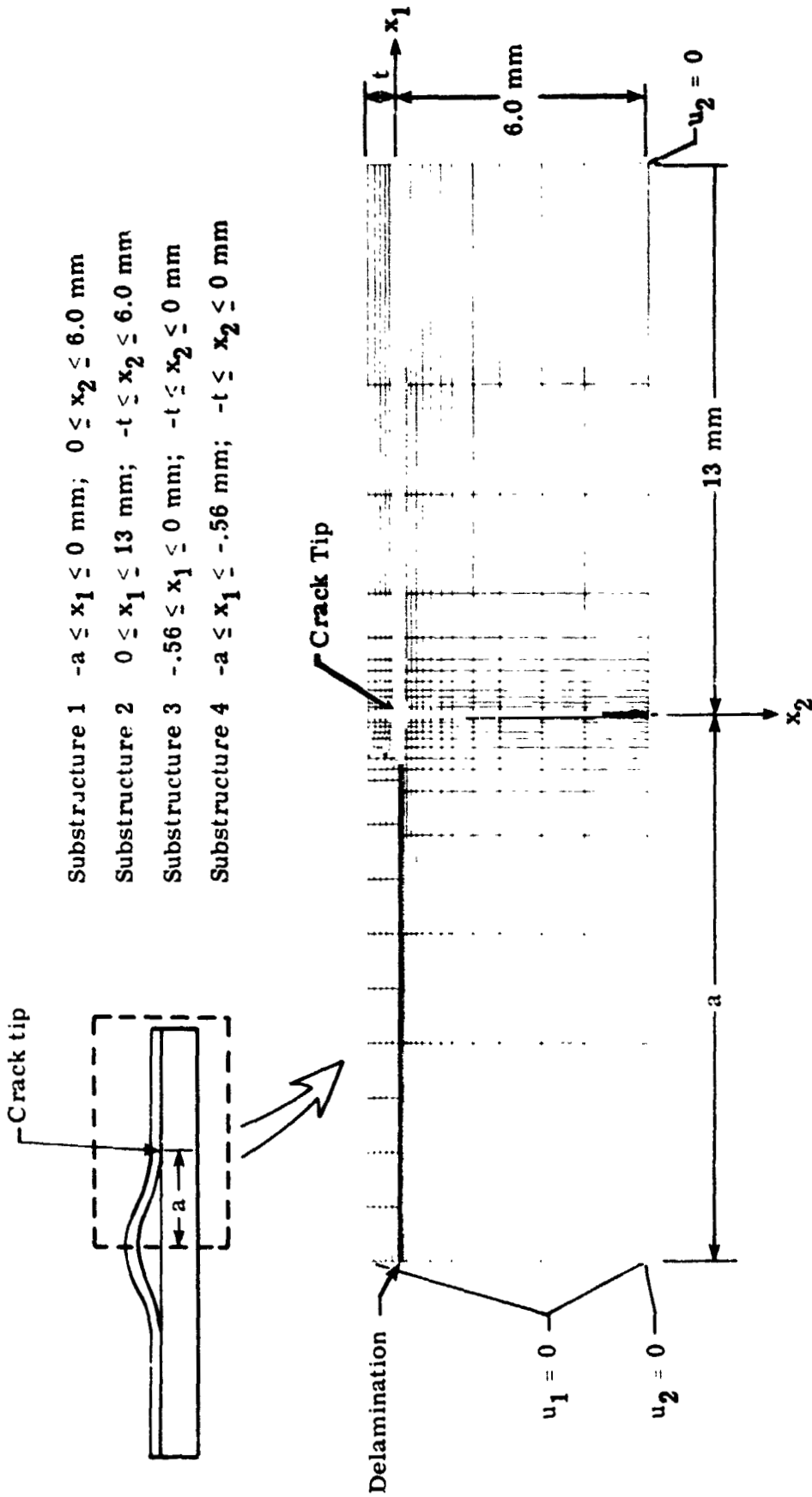
Figure 4.- Typical finite element mesh for parametric analysis.

(In this case $2a = 25$ mm, $t = .76$ mm.)

29
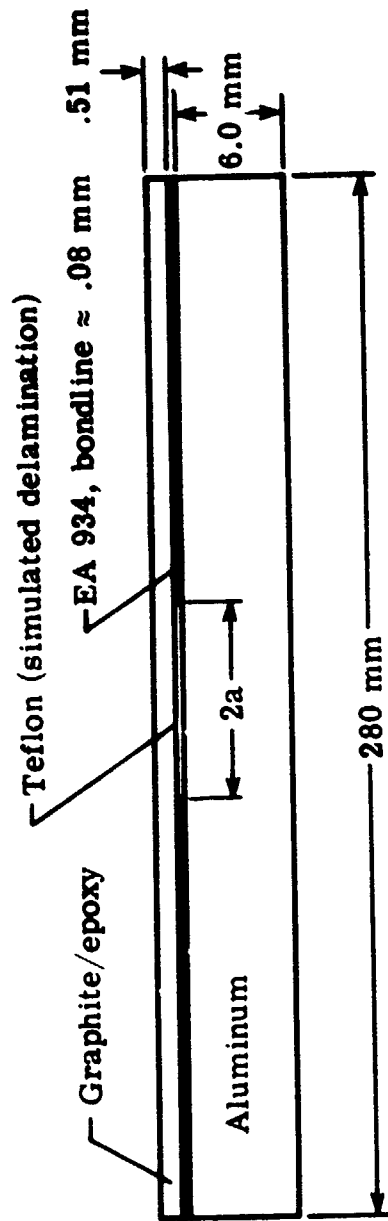
Figure 5.- Specimen configuration.
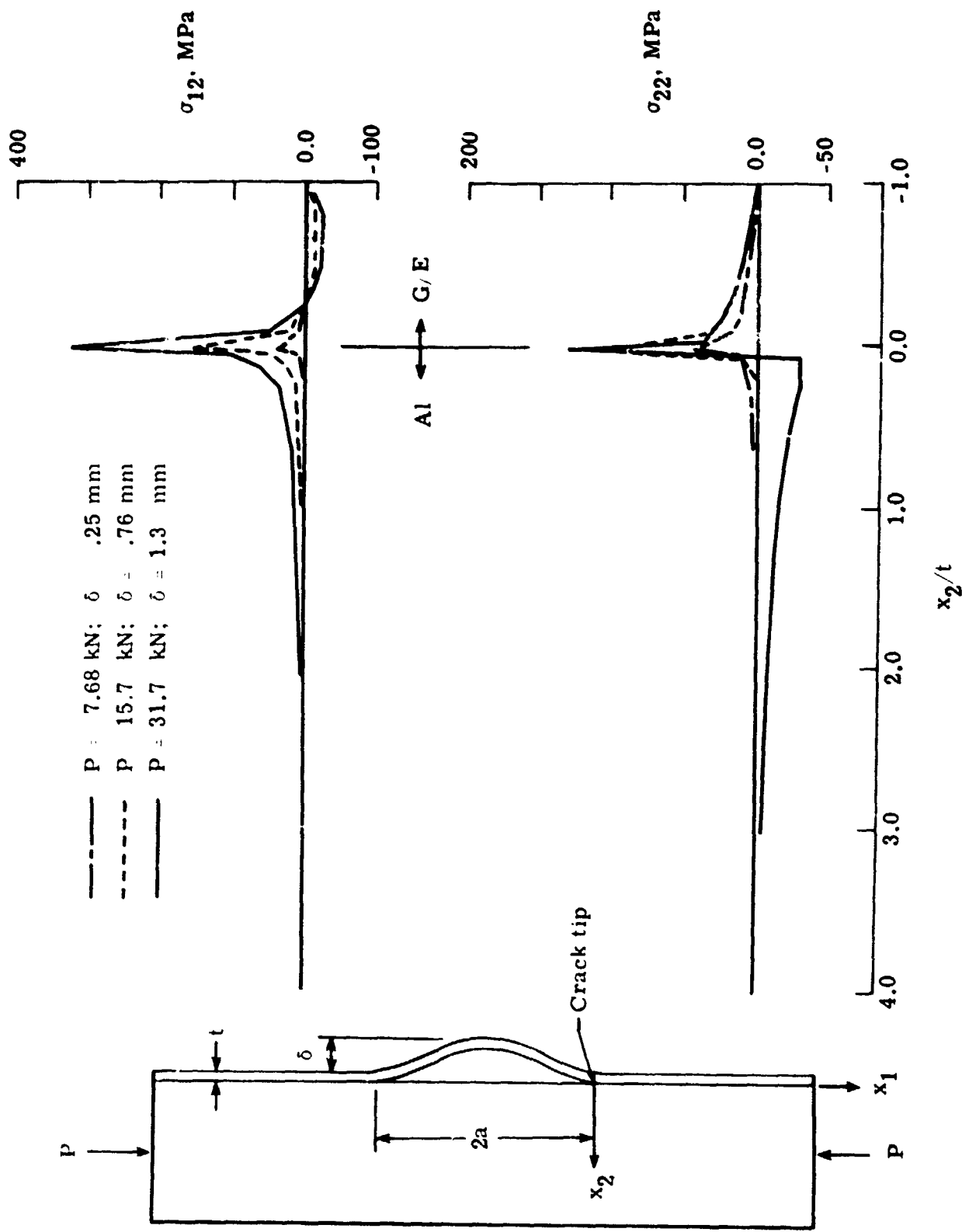
Figure 6.- Interlaminar stresses for buckled plies along X_1 = .0051 mm

(t = .51 mm, 2a = 38 mm)
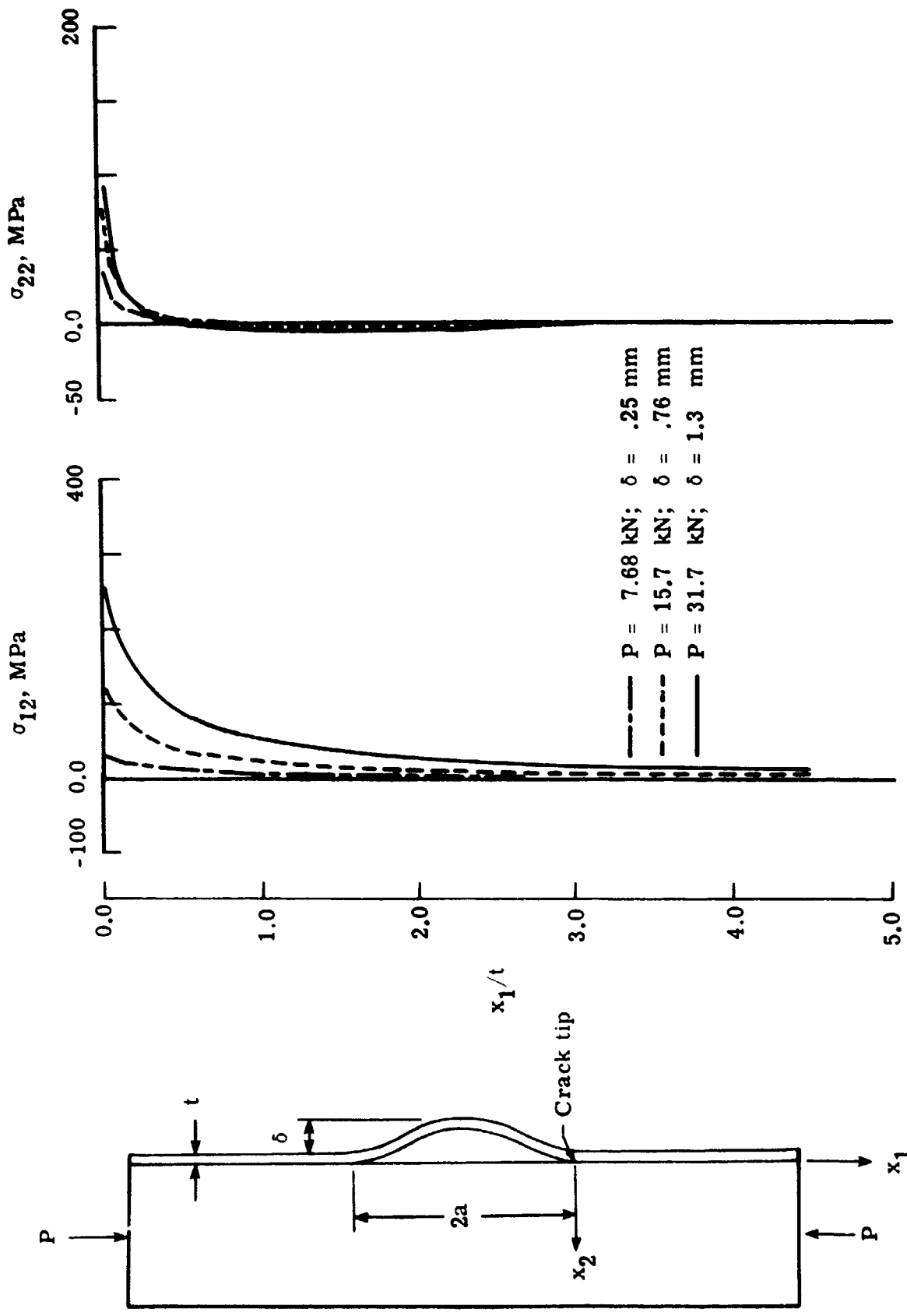
Figure 7.- Interlaminar stresses for buckled plies along $x_2 = 0$ (t = .51 mm, 2a = 38 mm).
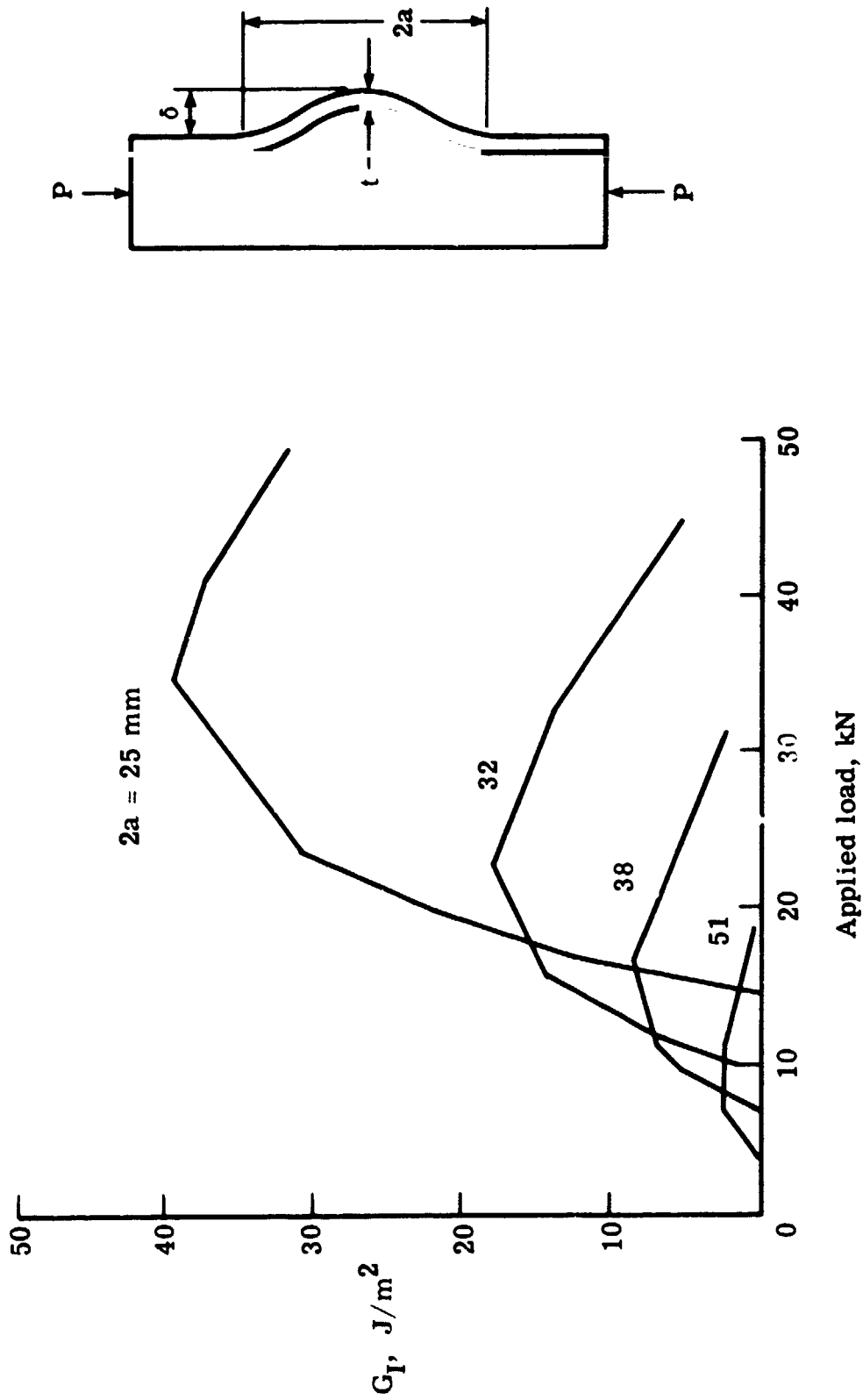
Figure 8. - Relationship between delamination length, load, and G_I (t = .51 mm).
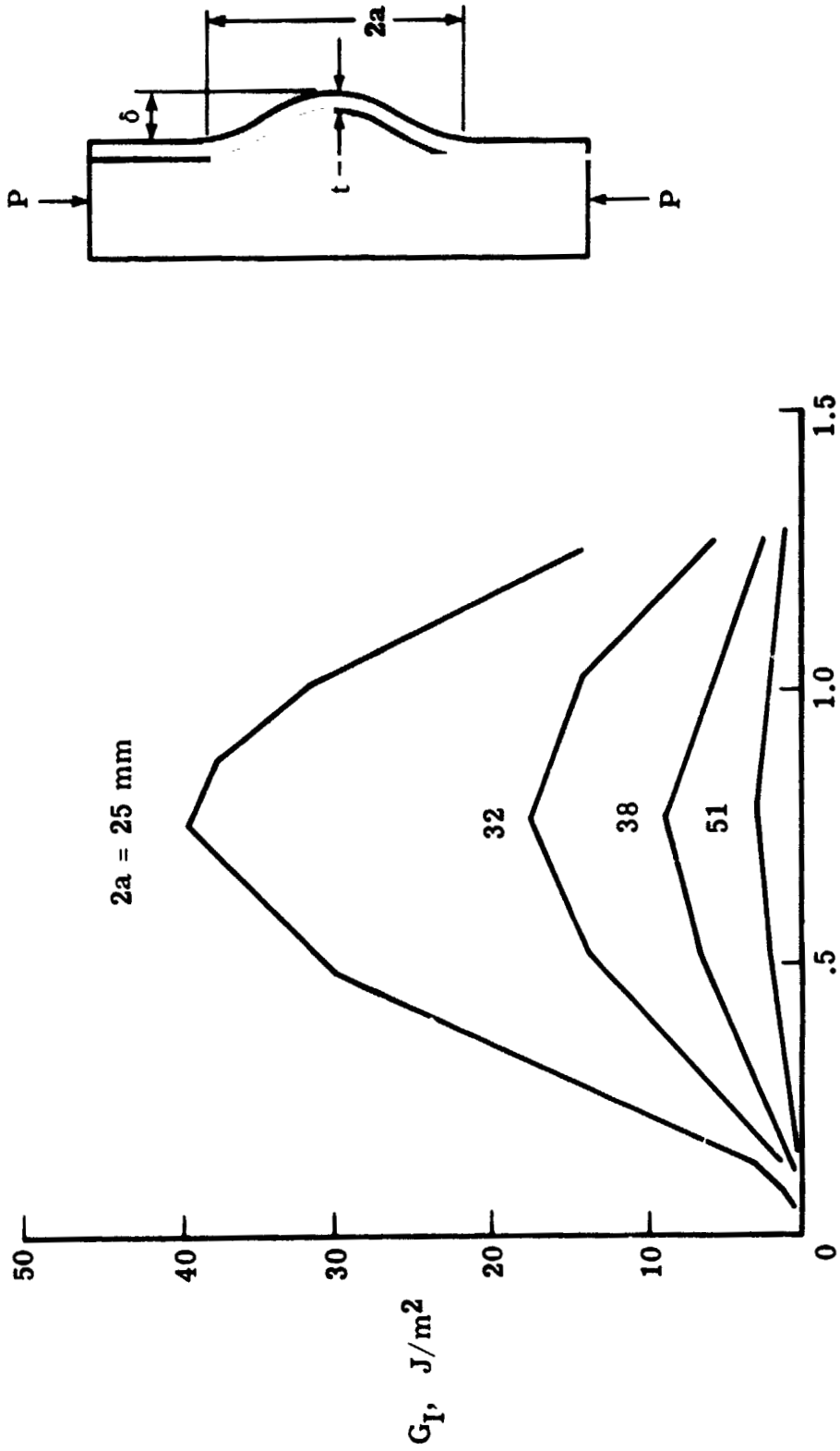
Figure 9.- Relationship between delamination length, lateral deflection, and G_I (t = .51 mm).
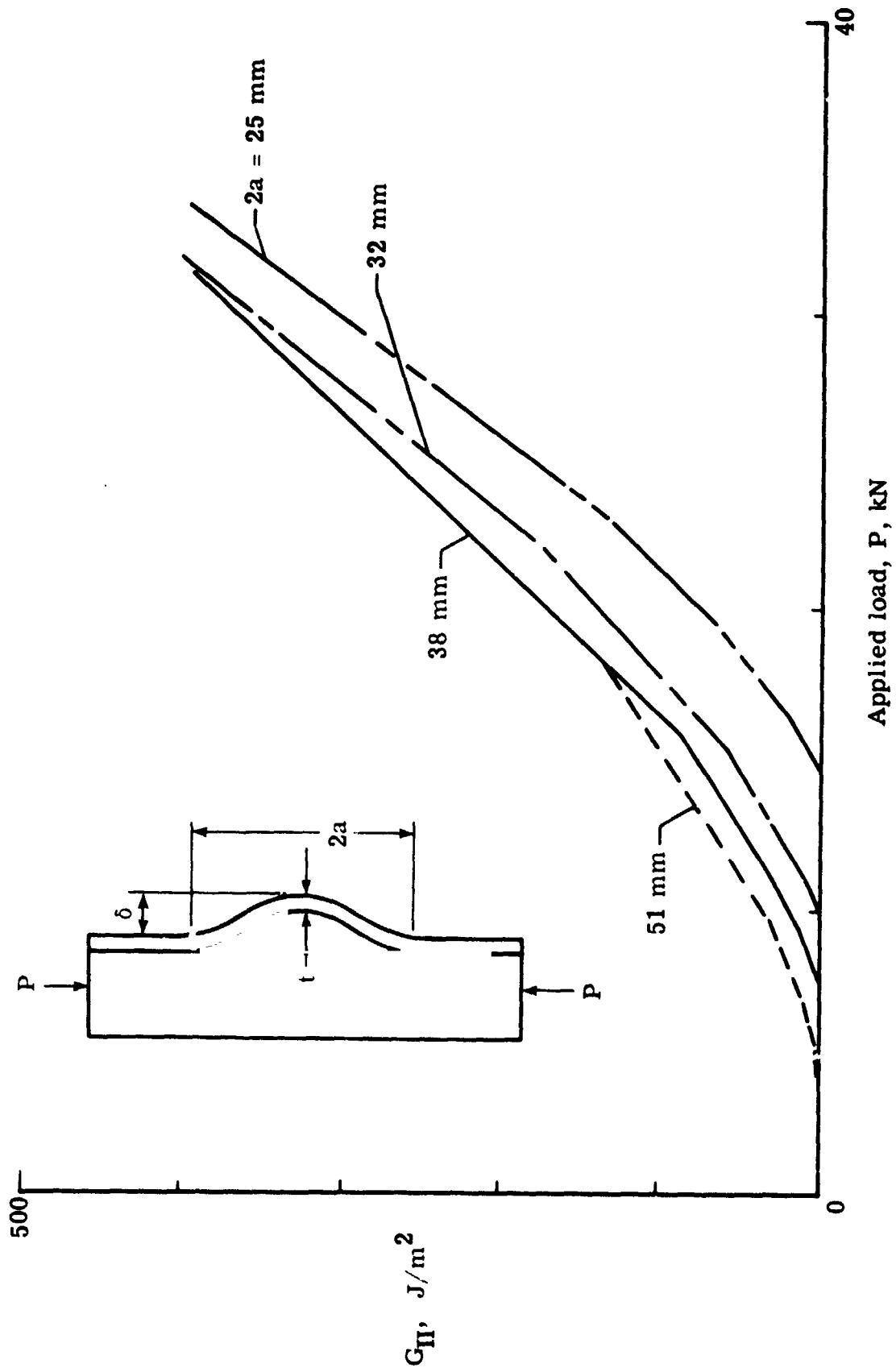
Figure 10.- Relationship between delamination length, load, and G_{II} (t = .51 mm).
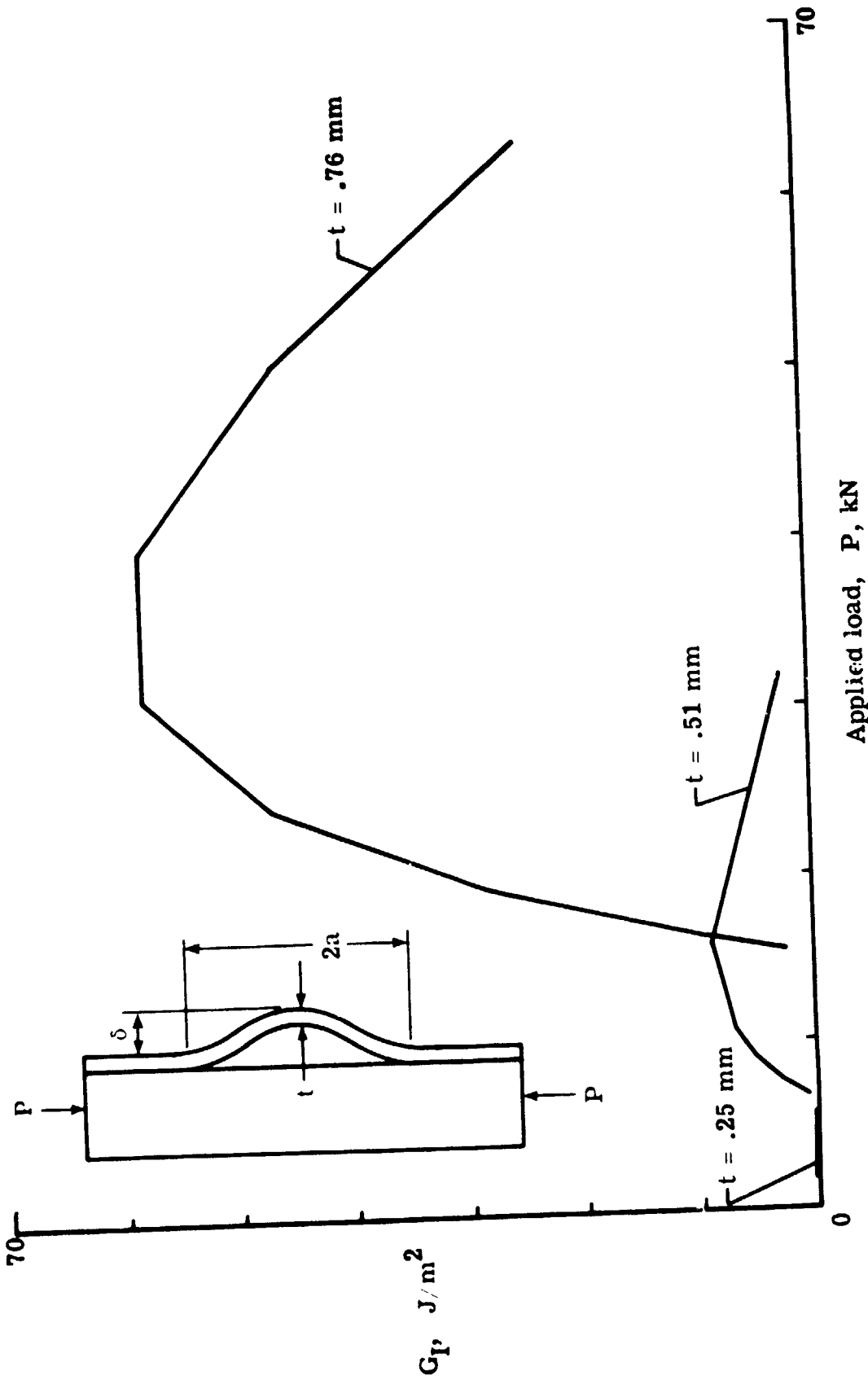
Figure 11.- Effect of delamination depth and load on G_I (2a = 38 mm).
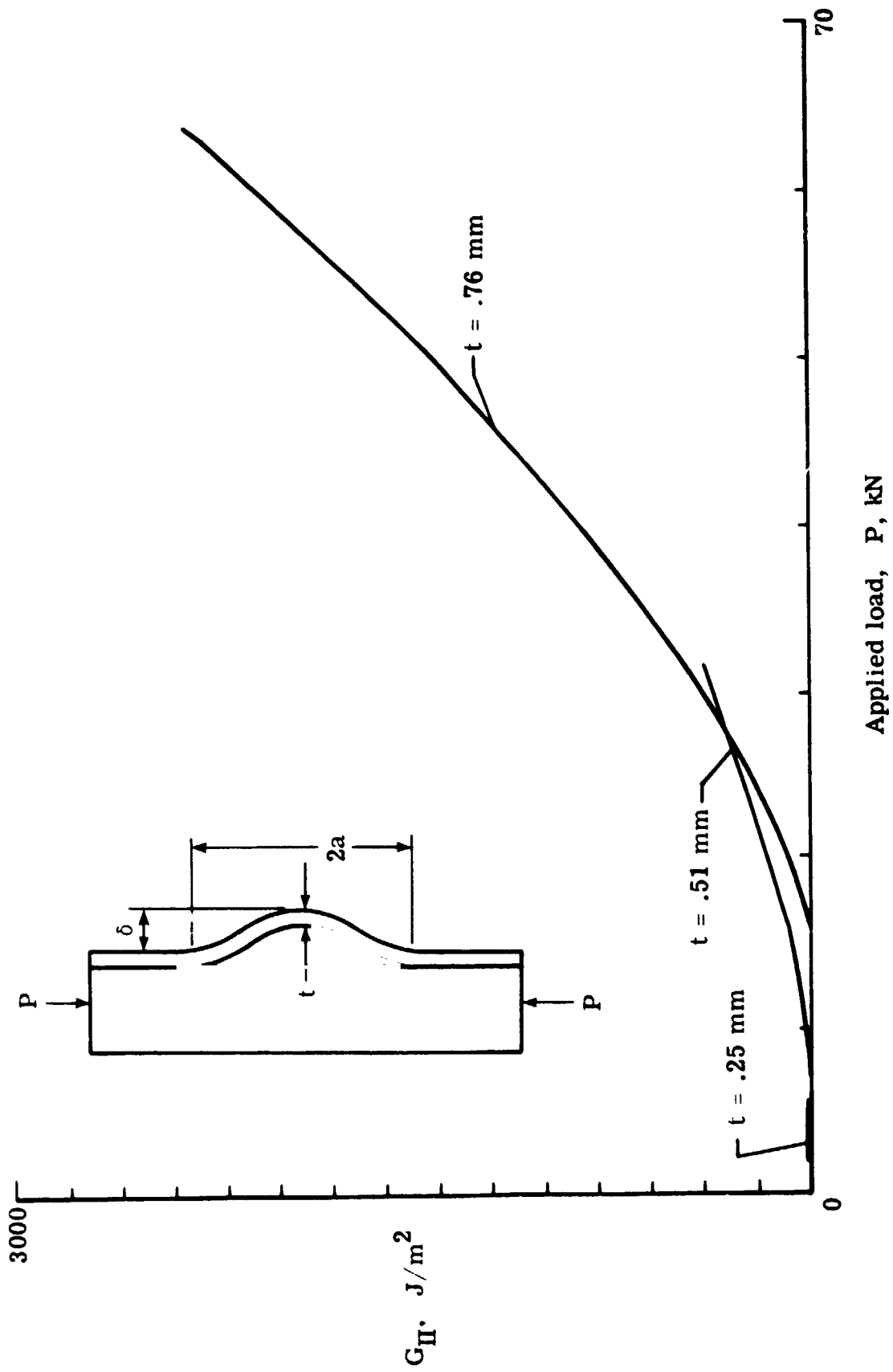
Figure 12.- Effect of delamination depth and load on G_{II} (2a = 38 mm).

37
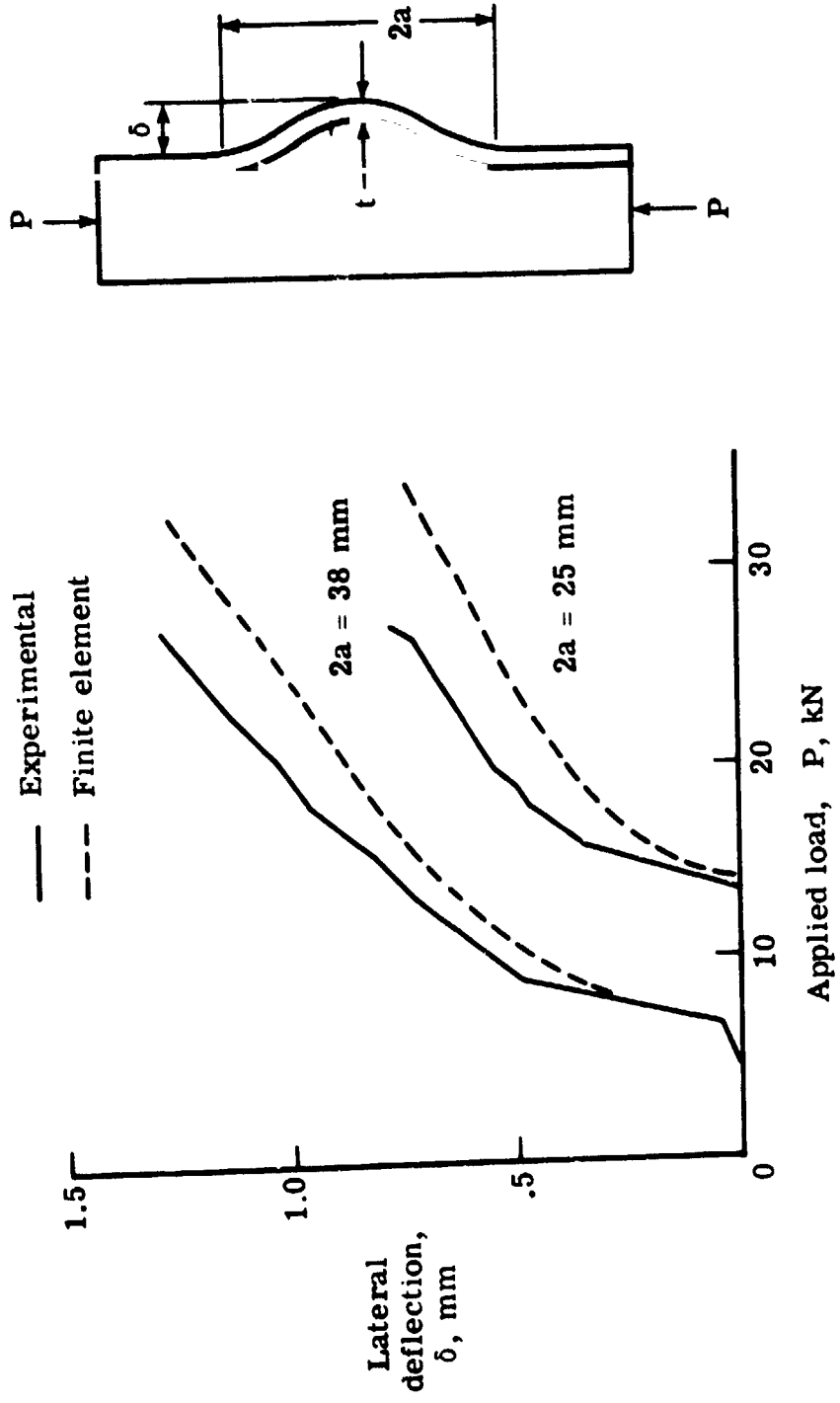
Figure 13.- Comparison of calculated and measured lateral deflections (t = .51 mm).
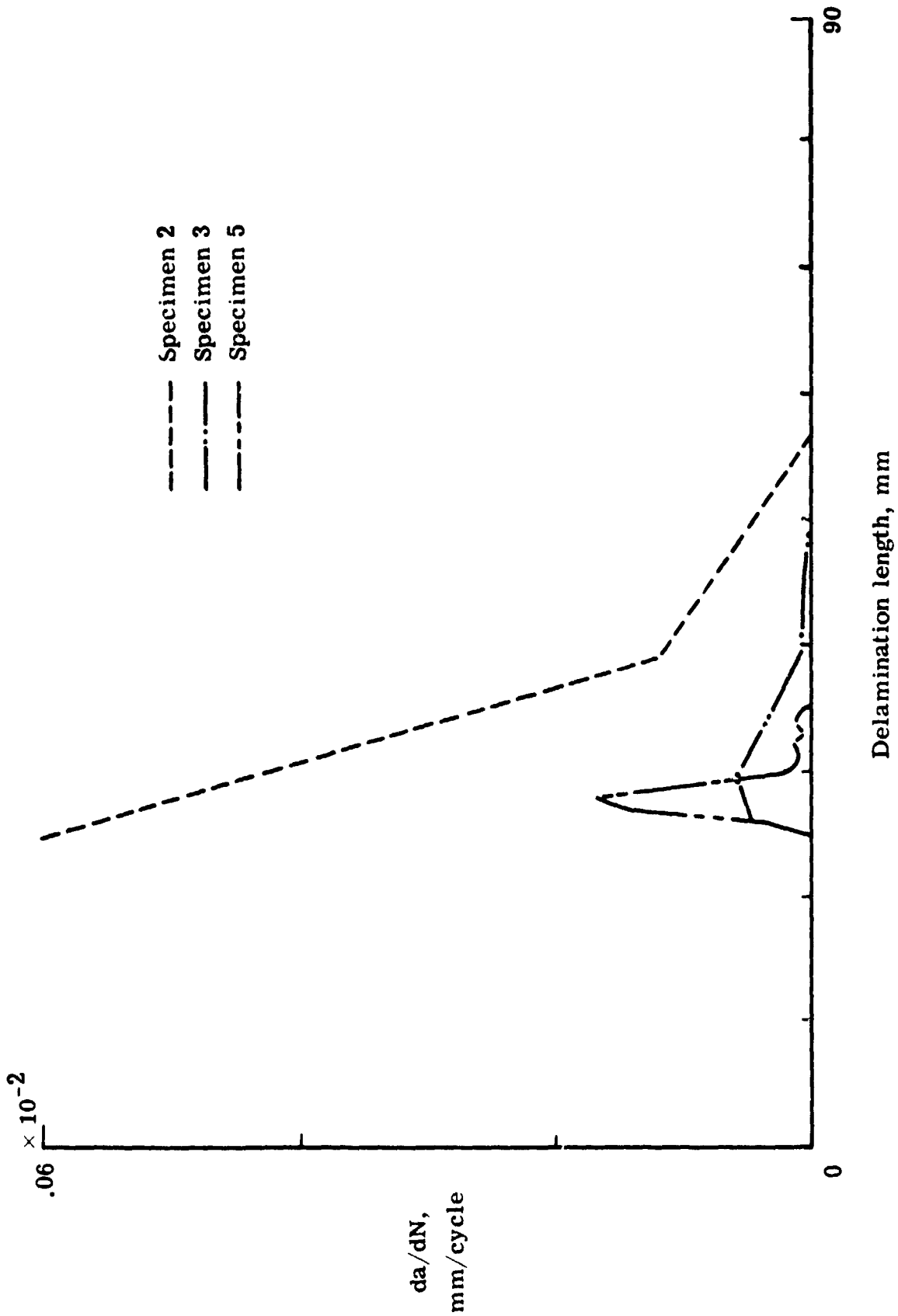
Figure 14.- Effect of delamination length and load on growth.

(a) P = 17.8 kN

39

da/dN,
mm/cycle

2×10^{-2}

Specimen 1
Specimen 2
Specimen 3
Specimen 4

Delamination length, mm

0   90
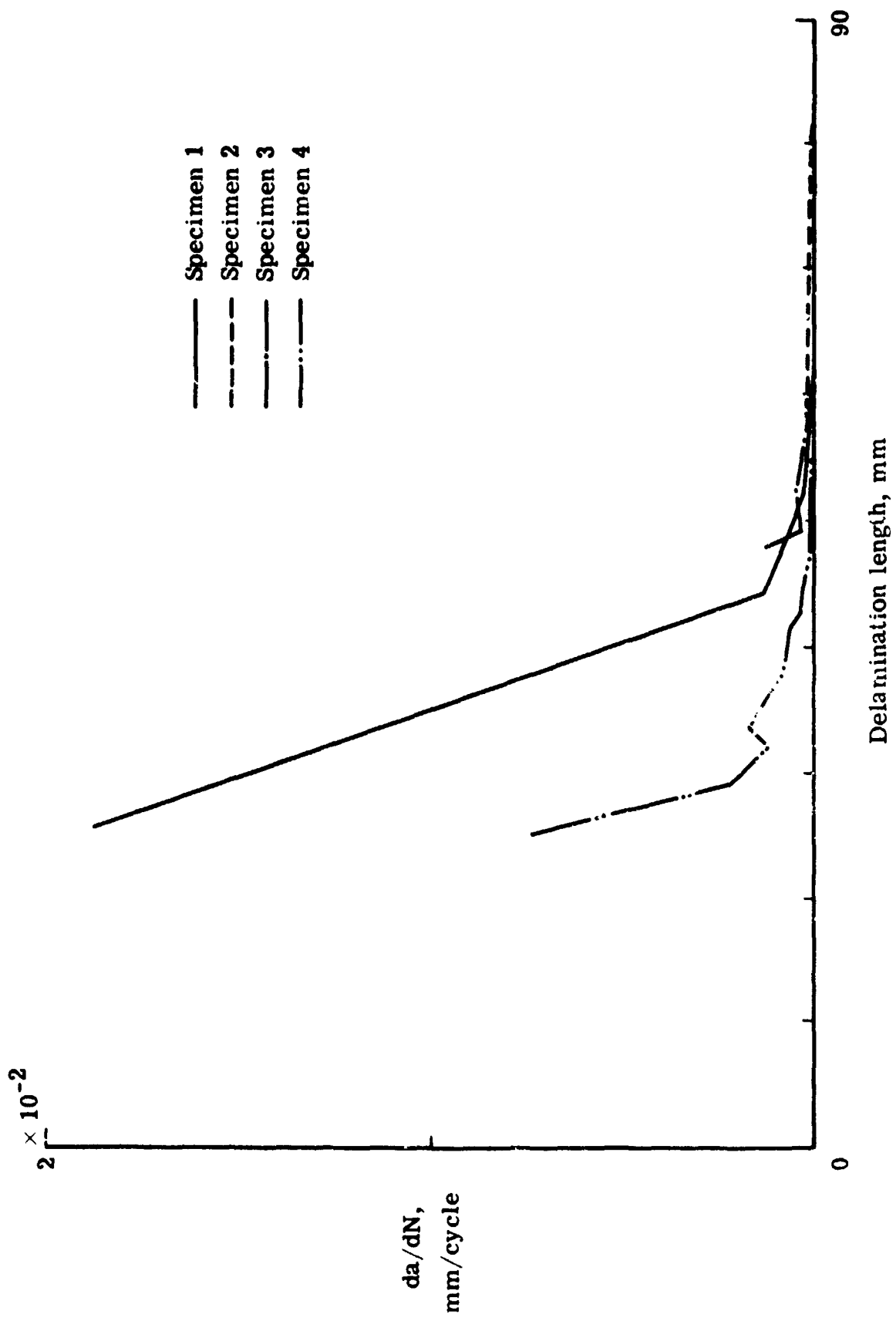
(b) P = 26.7 kN

Figure 14.- Concluded.

40
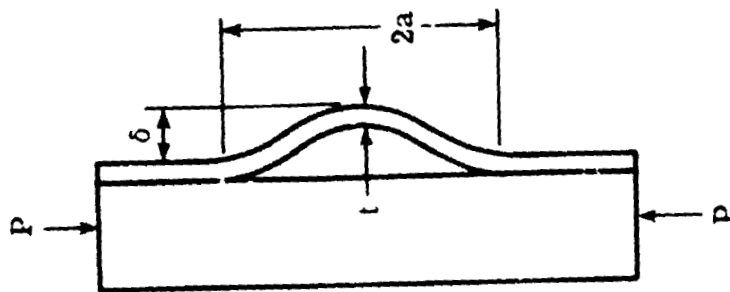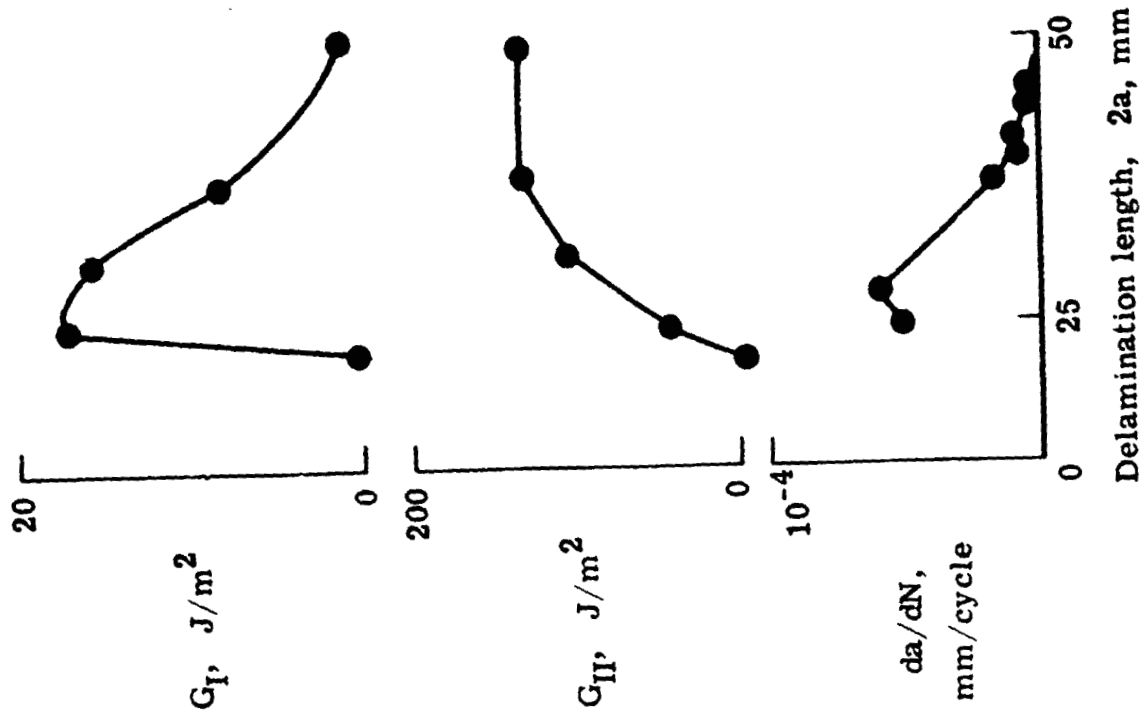
Figure 15.- Comparison of calculated strain-energy-release rates and measured delamination growth rates (t = .51 mm, P = 17.8 kN).
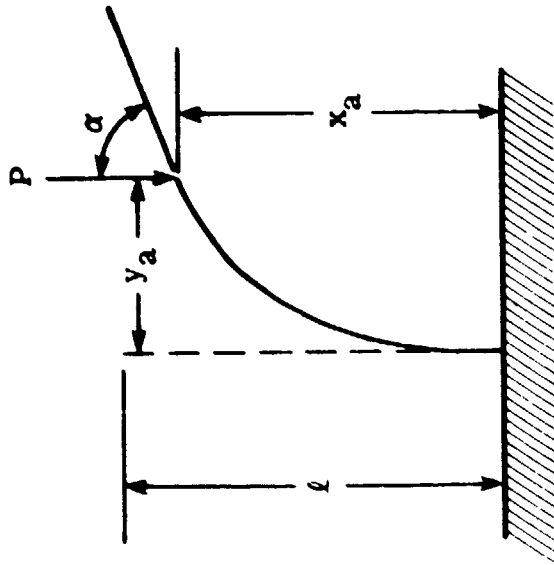
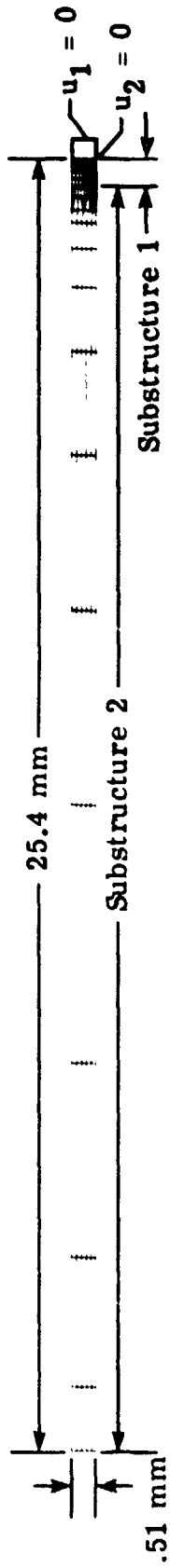Figure B1. - Column subjected to large deflection.

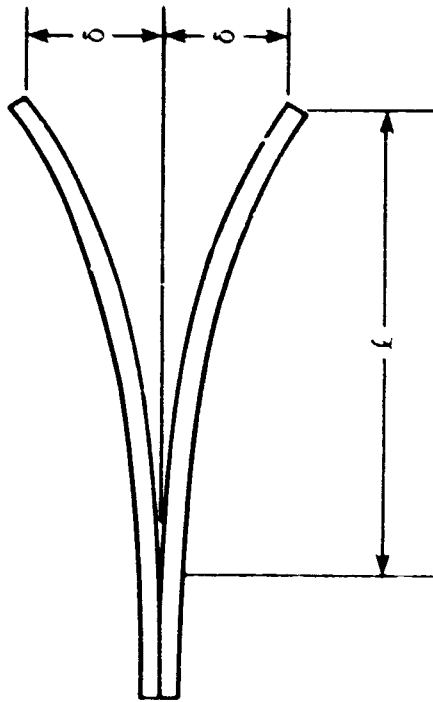Figure B2.- Finite element mesh for column and double cantilever beam problems.

Figure B3. - Double cantilever beam.